Acta Geotechnica
https://doi.org/10.1007/s11440-020-01117-1

RESEARCH PAPER

Fabric evolution and crack propagation in salt during consolidation and cyclic compression tests

Xianda Shen[1] · Jihui Ding[2] · Ilia Lordkipanidze[3] · Chloé Arson[3] · Judith S. Chester[4] · Frederick M. Chester[4]

Received: 18 April 2020 / Accepted: 12 November 2020

Abstract
It is of great interest to describe and quantify the evolution of microstructure for a better understanding of rock deformation processes. In this study, 2D microstructure images of salt rock are analyzed at several stages of consolidation tests and cyclic compression tests to quantify the evolution of the magnitude and orientation of solidity, coordination, local solid volume fraction, and crack volume. In both the consolidation and the cyclic compression tests, the deformation of aggregates achieved by grain rearrangement is greater than that achieved by the deformation of an individual grain. In the consolidation test, the aggregates are rearranged into horizontal layers of coordinated grains, the orientation distribution of grain indentations is quasi-uniform, and the size of the pores reduces and becomes more uniformly distributed. As a result, salt rock microstructure becomes more homogeneous. The increase in local solid volume fraction in the lateral direction is correlated with an increase in the oedometer modulus. In the cyclic compression tests, grain-to-grain contact areas decrease due to the redistribution of grains and the propagation of intergranular cracks. Aggregates are reorganized into columns of coordinated grains. Intergranular opening-mode cracks tend to develop in the axial direction, while intergranular shear-mode cracks propagate preferentially in the lateral direction. The lateral components of the fabric tensors of coordination and local solid volume fraction decrease, which result in an increase in the Poisson's ratio. The fabric descriptors used in this work allow a better quantification and understanding of halite deformation processes and can be used in other types of rocks encountering similar deformation mechanisms.

Keywords Cracks · Consolidation test · Cyclic compression test · Fabric · Grain contacts · Salt rock

1 Introduction

Salt rock (halite) is a polycrystalline material made of bonded crystals, also called grains. It is a favorable host material for geological storage of hydrocarbons, compressed air, carbon dioxide and radioactive waste, because of its low permeability and ideal creep properties [5, 21, 26, 54]. Understanding how halite microstructure evolves during a variety of loading paths is of foremost importance to predict the long-term behavior of salt rock around storage facilities [25, 38, 47]. Previous studies show that salt rock local deformation is controlled by the direction of grain-to-grain contacts and by the packing of grain aggregates [36, 37, 42]. Frictional sliding at grain boundaries is the primary accommodation mechanism at room temperature, under low confining pressure and under high strain rate. Deformation is controlled by the normal and shear stresses at grain boundaries and by the distribution of boundary orientations [8]. The rate of diffusional sliding depends on the shape of the grain boundaries [35]. State-of-the-art salt mechanics is informed by cavern stability analyses (at a scale of 1–10 m and above) and by microscopic observations (at the sub-millimetric scale). Continuum models of salt, at a scale of 0.01–1 m, are based

✉ Xianda Shen
xianda.shen@northwestern.edu

[1] Department of Civil and Environmental Engineering, Northwestern University, Evanston, IL, USA

[2] Department of Geophysics, Stanford University, Stanford, CA, USA

[3] School of Civil and Environmental Engineering, Georgia Institute of Technology, Atlanta, GA, USA

[4] Center for Tectonophysics, Department of Geology and Geophysics, Texas A&M University, College Station, TX, USA

Published online: 02 January 2021

on empirical creep power laws or phenomenological assumptions based on qualitative observations (e.g., the dilatancy boundary) [3, 4]. By contrast, fabric tensors provide a quantitative description of rock microstructure. Although fabric is a common measure used for characterizing fractured rock and granular media, in which macroscopic stiffness and strength are sensitive to the topology of the internal microscopic structure, fabric was never assessed quantitatively at the scale of a representative elementary volume (REV) of salt rock. That is why in the present study, we analyze the response of salt rock by means of fabric tensors, defined as functions of probability distribution of independent geometric descriptors [14, 30, 56].

Fabric is influenced by both internal microstructure prior to loading and the applied stress path [41, 46]. Recently, various morphological descriptors were proposed to understand the internal microstructure of granular materials. Guida et al. [17]) conducted a fractal analysis of the 2D contour of particles to define morphological descriptors at the macro-, meso-, and micro-scale. Two-dimensional size and shape descriptors (i.e., dimension, aspect ratio, convexity, roundness) were correlated to 3D morphological indexes [43, 55]. Lai and Chen [24] applied machine learning techniques and an edge-based level-set method to reconstruct realistic 3D particle shapes and analyze particle morphology through sphericity, roundness, and roughness. All of these studies focus on the intrinsic shape of particles and do not account for the anisotropy exhibited by granular assemblies. In granular materials, mechanical anisotropy is mainly due to the shape of pores and particles (grains) and to the distribution of the contact normal orientations [31]. Triaxial tests performed on Toyoura sand and rice grain specimens [52] showed that stiffness anisotropy is more pronounced in specimens with elongated grains. Triaxial tests conducted on circular and elongated rods [30] and on natural sands [50] demonstrated the effects of the geometry and orientation of grains on the anisotropy of strength in granular materials. In rock, a correlation was found between the anisotropy of macroscopic elastic properties and strength on the one hand, and the directional distribution of contact orientations on the other hand [34]. X-ray micro-CT scanning has recently emerged as a powerful technique to characterize fabric in geomaterials [53]. However, salt is a monomineralic rock that is difficult to image based on the heterogeneity of density in a specimen. In the present study, we thus base our fabric analysis on microscopy images, a technique that provided significant insights on fabric evolution and ensued deformation in a variety of geomaterials [20, 33, 49], including salt crust [10].

In this paper, we analyze 2D halite microstructure images acquired at several stages of consolidation tests and cyclic compression tests. We calculate the magnitude and orientation distributions of solidity, local solid volume fraction, coordination orientation and crack volume fraction, and we define the associated fabric tensors to explain the development of anisotropic mechanical properties. Our methods for analyses are explained in Sect. 2. The distributions of fabric descriptors and crack densities are presented in Sect. 3. In Sect. 4, we interpret the development of intergranular opening-mode and intergranular shear-mode cracks in the cyclic compression tests. We conclude the paper by comparing the evolution of the components of the fabric tensors to that of halite elastic moduli.

2 Materials and methods

2.1 Consolidation tests and cyclic compression tests

Reagent-grade granular salt (99 wt%) was used in consolidation tests. Before consolidation, granular salt was sieved to produce more uniform grain sizes of 0.3–0.355 mm diameter. Uniaxial consolidation of granular salt was conducted in a hollow cylindrical steel vessel at a temperature of 150 °C. Consolidation of salt grains was achieved by confining rigid lateral steel boundaries and advancing a piston in the axial direction at a displacement rate of 0.034 mm/s [12, 39]. Repeat tests were conducted and stopped at different maximum axial loads to obtain samples of varying porosities, i.e., 3%, 5%, 10%, and 15%. These samples were then prepared to make petrographic sections, chemically etched, and imaged using an optical microscope. Figure 1 shows the binary images of consolidated samples taken from sample centers in axial sections.

Cyclic compression tests were conducted on consolidated samples with an initial porosity of 5% ± 0.5%. Consolidated samples were deformed in a triaxial apparatus at a confining pressure of 1 MPa, at room temperature [13]. Repeat tests were conducted at the same conditions and stopped at different axial strains to obtain samples at varying deformation stages, i.e., axial strains of 0.8%, 1.8%, 2.8%, 3.8%, and 7.3%. Figure 2 shows the binary images of triaxially deformed samples taken from sample centers in axial sections.

2.2 Grain morphology

Grain morphology refers to the size and shape of an individual grain. Fabric descriptors such as projected areas, Feret diameters and effective grain diameters all characterize grain size [1, 7, 18]. Roundness [9, 22], aspect ratio [44] and sphericity [22, 51] describe grain shape.

In order to analyze the evolution of grain size and shape during the consolidation and cyclic compression tests, we

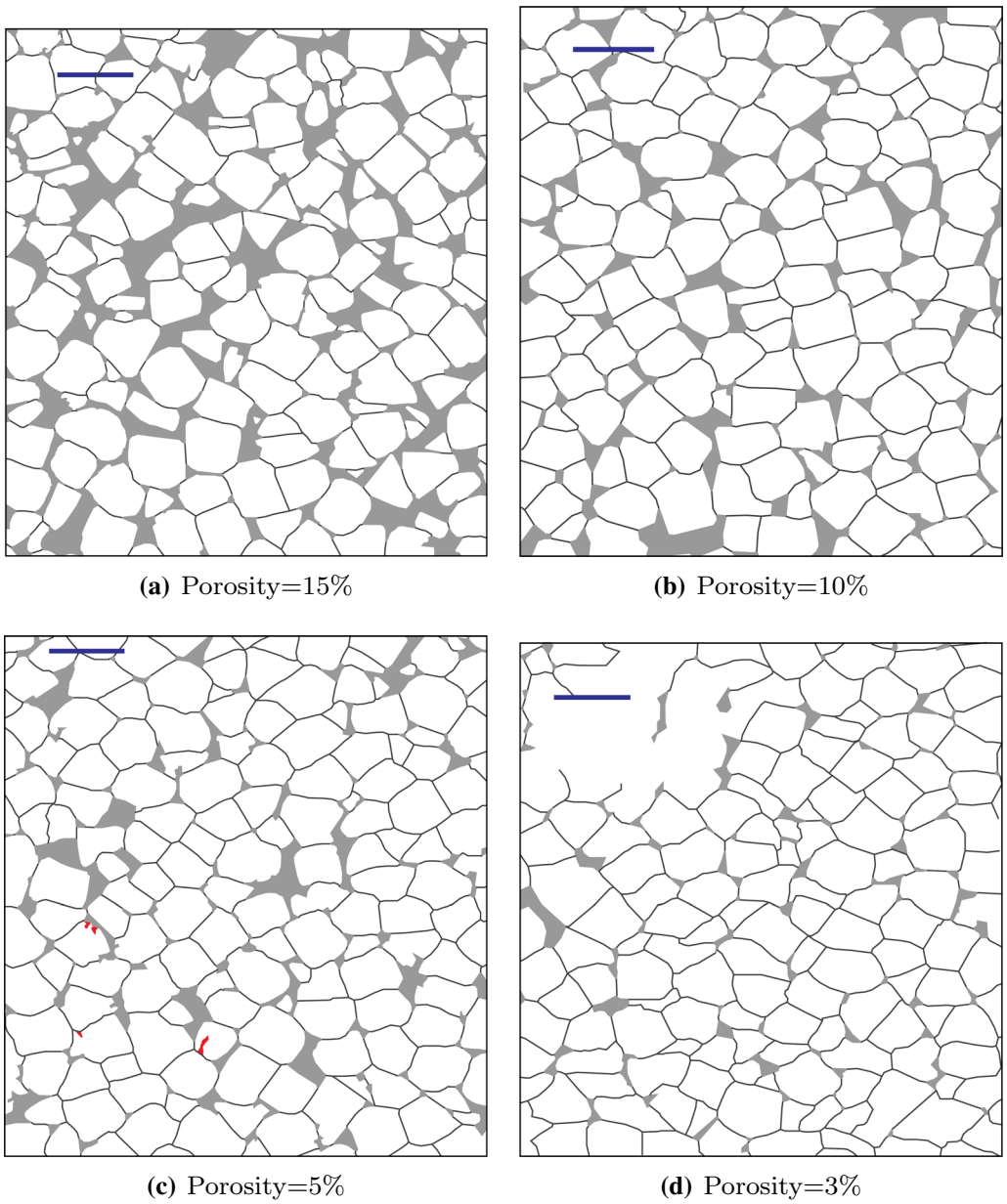

Fig. 1 Binary images of salt microstructure at several stages of consolidation tests. The blue scale bar represents 0.5 mm. The red inserts indicate the presence of intragranular cracks (see Sect. 2.3.3)

first process the images to associate an equivalent ellipse to each grain that appears in the images. An equivalent ellipse has the same second moments of area (i.e., respective to horizontal and vertical axes) as the associated grain in the 2D image. The orientation of a grain is defined as the angle between the major axis of the equivalent ellipse and the horizontal direction (note: the loading direction is vertical).

We seek to explain salt behavior from a higher-order descriptor of the contours of grains—called grain solidity. Solidity is usually defined as the ratio between the area of a grain image by the area of the convex hull of the grain. When solidity is close to one, grains have convex shapes. A solidity close to zero reveals a very angular shape or a shape with very rough contours. In the images obtained in this study (Figs. 1 and 2), the lack of convexity stems from indentations that appear at the contour of the grains.

In order to better understand how grain indentations develop, we define an anisotropic descriptor of solidity. The norm of a solidity vector is the ratio of the area of the 2D image of a grain by the area of its convex hull. The direction of the solidity vector is calculated as follows:

(i) Indentations around each grain are identified by observing the microstructure binary images—see the example shown in Fig. 3.

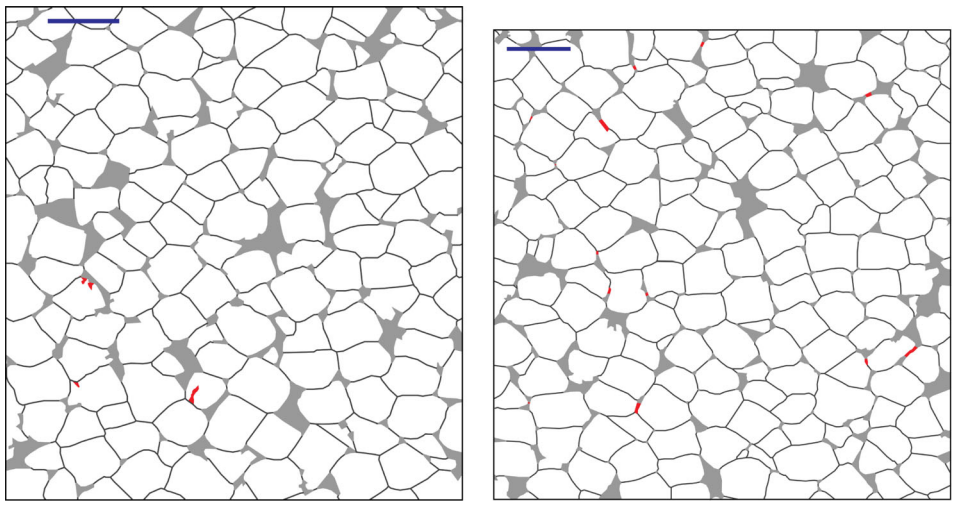

(a) $\epsilon_a = 0\%$ **(b)** $\epsilon_a = 0.8\%$

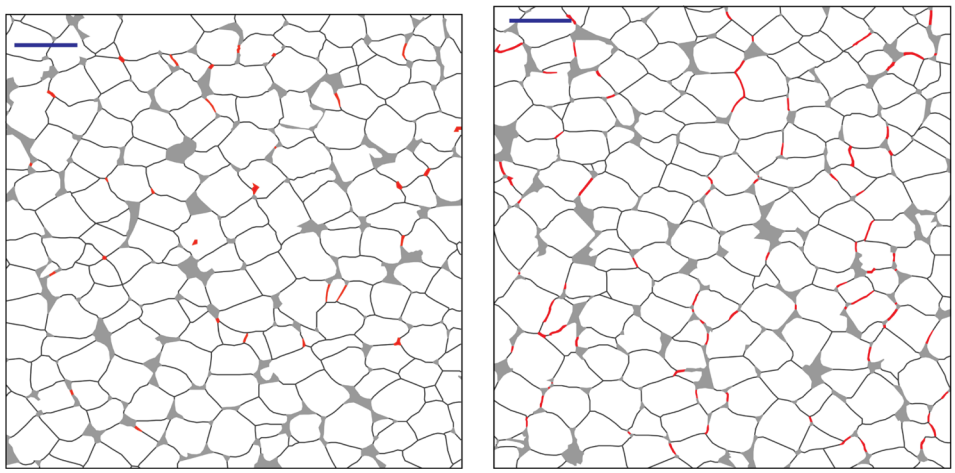

(c) $\epsilon_a = 1.8\%$ **(d)** $\epsilon_a = 2.8\%$

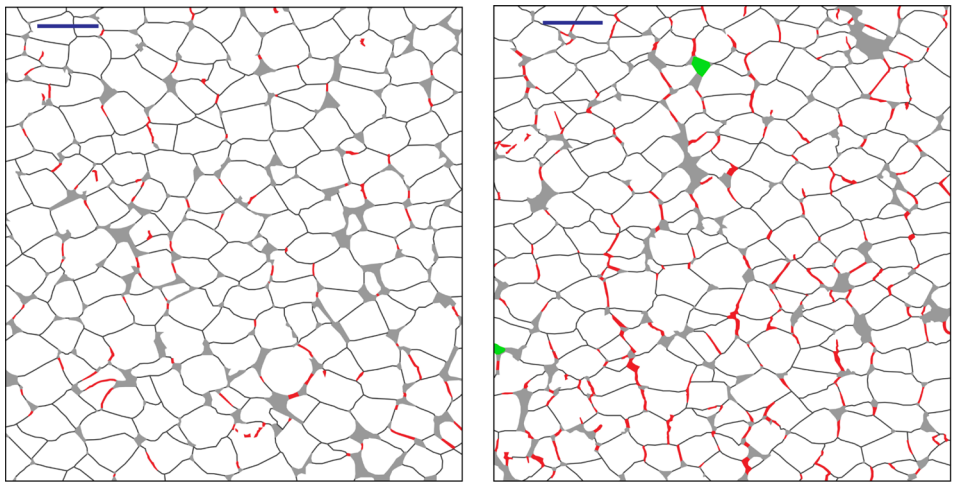

(e) $\epsilon_a = 3.8\%$ **(f)** $\epsilon_a = 7.3\%$

Fig. 2 Binary images of salt microstructure at several stages of cyclic compression tests. The blue scale bar represents 0.5 mm. The red inserts indicate the presence of cracks (see Sect. 2.3.3). The green areas represent grains that were removed by polishing

(ii) An algorithm calculates the position of the barycenter of each indentation shape, as well as that of the grain. For each indentation, a segment linking the indentation center to the center of the associated grain is defined.
(iii) The angle to the horizontal of each segment defined in step (ii) is calculated. Angles are defined over the interval [0°;90°] because of the axial symmetry of the tests.
(iv) For each grain, the direction of the solidity vector to the horizontal is the mean of the angles calculated in step (iii), in which each angle is weighted by the area of the associated indentation.

2.3 Grain arrangement

In addition to the descriptors of grain morphology, many descriptors were proposed to characterize grain arrangement. The void ratio is a parameter measuring the packing density of granular materials at the macroscopic scale. Based on the concept of void ratio, the local void ratio distribution was proposed to measure volumetric changes at the microscopic scale [2, 15, 23]. Within a 2D image, the local void ratio is calculated over polygonal sub-domains, in which polygon corners are grain centroids. The coordination number of a grain is equal to the number of grains that are in contact with that grain. It is usually defined as the average number of contacts per grain. Based on this definition of the coordination number, many contact fabric parameters were proposed to discriminate grains with less contacts [29, 45] or to measure the area of grain contacts [32]. Distributions of directional descriptors are typically determined by stereological methods [19]. Descriptors of magnitude such as volumetric fraction, coordination number, grain size distribution, and crack density define the trace of fabric tensors [28].

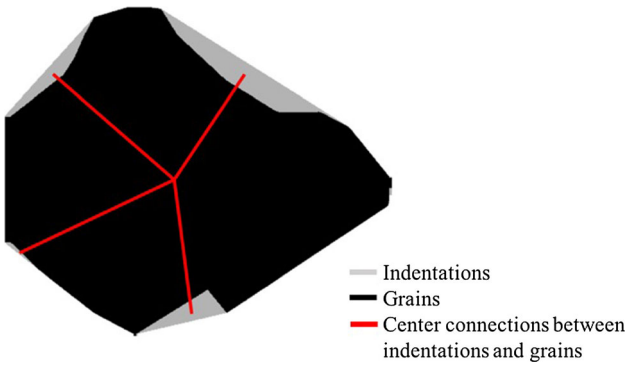

Fig. 3 Processed binary image of a grain, showing indentations on the contour. The image was taken at an axial strain 0%, before the cyclic compression tests

2.3.1 Coordination orientation

The coordination number is defined as the number of grain-to-grain contacts at the surface of a given grain. We define a coordination descriptor that also accounts for the area of the contacts, as well as the orientation of the vectors normal to the contacts. The so-called coordination orientation is calculated by image analysis, as follows:

(i) The pixels that make the contour of a grain are listed. Pixels that are at the boundary with another grain (named "boundary pixels") are then selected from that list.
(ii) Segments that link the center of the grain to its boundary pixels are defined. The angles formed by these segments to the horizontal are calculated.
(iii) The contour of the grain is divided into 360 angular equal segments (Fig. 4). For each contour segment within one of the 360 angular segments, the ratio of the number of boundary pixels to the total number of pixels is calculated, which provides a quantitative measure of the support fraction on that segment.
(iv) The coordination orientation of a grain is the average orientation of the angular segments, weighted by their support fraction.

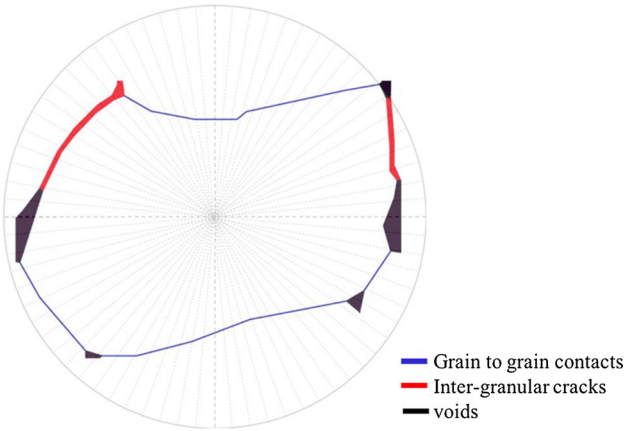

Fig. 4 The method to calculate the coordination vector of a grain. The contour of the grain is divided into 360 equal angular segments. (This sketch only presents 72 intervals for clarity.) The orientation of the coordination vector of the grain is calculated as the averaged orientation of the grain-to-grain contacts intervals. The magnitude of the coordination vector is the fraction of the grain-to-grain contacts intervals to the contour of the grain

2.3.2 Local solid volume fraction

In order to quantify the heterogeneous distribution of voids in the salt sample, we define the local solid volume fraction (LSVF) vector as follows:

(i) Contact branches, defined as segments linking the centers of two grains in contact, are plotted. A map of polygons is obtained, as shown in Fig. 5a. Polygon corners are grain centers.
(ii) The solid volume fraction of the domain contained in each polygon is calculated.
(iii) Segments are defined to connect each grain center to the centers of each polygon that overlaps with that grain. The angle between a segment and the horizontal defines the orientation of a polygon relative to a grain. The orientation of the connection is called "direction of the domain polygon";
(iv) The magnitude of LSVF of a grain is the total solid volume fraction of its domain polygons (Fig. 5b). The direction of the LSVF vector is the average of its domain polygons' directions, using the solid volume fraction of domain polygons as the weights.

2.3.3 Crack propagation during the cyclic compression tests

Intergranular cracks, often also referred to as grain boundary cracks, are the microscopic cracks that initiate and propagate along grain boundaries. By contrast, an intragranular crack is defined as a micro-crack that develops through only one grain. In the cyclic compression tests, opening-mode microscopic cracks were observed. With the increase in axial strain, salt grains re-arranged and intergranular cracks appeared. Intragranular cracks also occurred, because of stress concentration induced by grain contacts. In the following, the length and orientation distributions of both the intergranular and intragranular cracks are quantified.

3 Results

3.1 Consolidation tests

3.1.1 Grain morphology

The major axis of a grain is defined as the major axis of the equivalent ellipse of that grain. Similarly, the aspect ratio of a grain is defined as the ratio of the major axis to the minor axis of the equivalent ellipse of that grain. In the consolidation tests, the mean major axis of the grains was around 400 μm when the porosity of the samples was larger than 5% (Fig. 6). The aspect ratio of the grains remained under 2 until the porosity reached 3%, after which grains with a larger major axis appeared, i.e., grains became elongated.

Grain deformation affects grain anisotropy and grain rotation influences grain orientation, especially when the porosity of the specimen is low (i.e., 3% and 5%). According to Fig. 6, the distribution of grain aspect ratios

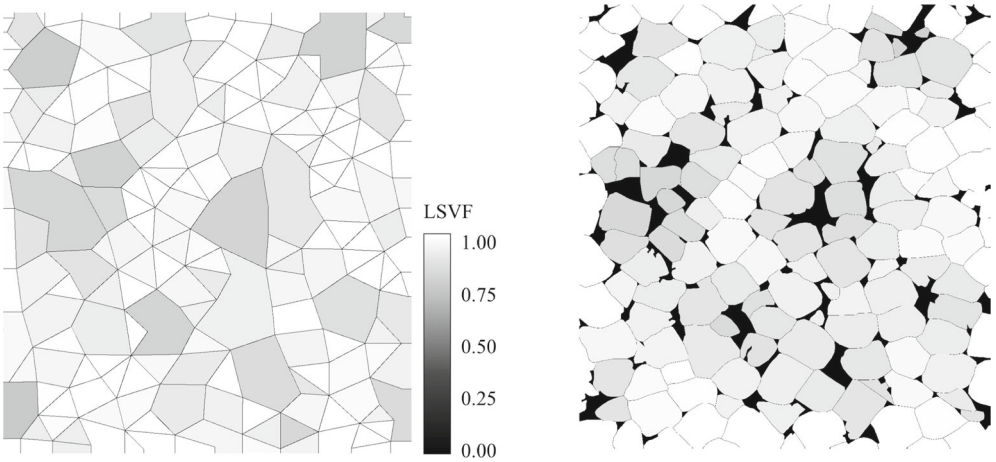

(a) Polygons delimited by contact branches **(b)** Solid volume fraction of grains

Fig. 5 The method to calculate local solid volume fraction of grains. The gray scale illustrates the differences in local solid volume fractions. The images were taken at an axial strain of 0%, before the cyclic compression tests. **a** The polygons map is constructed by plotting branches from grain centroid to grain centroid; local solid volume fraction is calculated for each polygon. **b** The area of the surface covered by the polygons that overlap with a grain is called the domain of this grain; the solid volume fraction of a grain is the averaged solid volume fraction of the domain of that grain

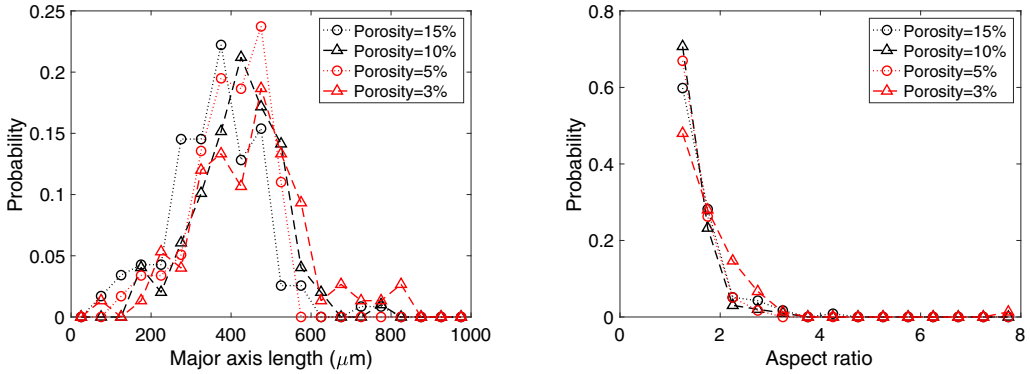

(a) Major axes of grains **(b)** Aspect ratios of grains

Fig. 6 Evolution of the shape of salt grains during the consolidation tests. The major axis of the grains increases during the consolidation process. At low porosity, grains with a larger aspect ratio appear in the specimen

stays the same throughout the consolidation test until the porosity of the specimen reaches 5%. This indicates that grains tend to deform and rotate to form horizontal layers of elongated grains under compaction (Fig. 7).

Compaction triggers grain indentations and grain plastic deformation. Solidity can be viewed as an average effect of grain indentation at the scale of the image processed. Initially, the solidity vector is oriented at an angle of 45^o in average, i.e., the orientation of the solidity vector is uniformly oriented between 0^o and 90^o in the sample (Fig. 8a). The decrease in the peak of orientation probability distribution indicates that the orientation of indentations on the grain surface becomes less uniformly distributed and that anisotropy develops in the specimen. More and larger indentations occur on the grain surface with the decrease in porosity (Fig. 8b). Plastic deformation accumulates in grains.

Grain deformation is induced by intragranular cracking and intragranular dislocation glide. The dominant process is most definitely dislocation glide, as evidenced by the development of dense arrays of dislocations and the rare occurrence of intragranular cracks. In the consolidation tests, dislocation glide dominates grain deformation, because of the elevated temperature and because of the low dislocation density in the original salt crystals at the beginning of the consolidation test [11].

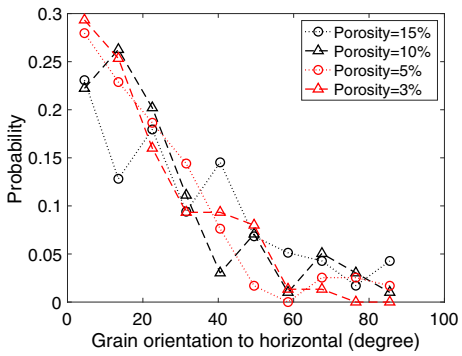

Fig. 7 Evolution of the orientation of the salt grains during the consolidation tests. The orientation of the major axis of the grains gets closer to the horizontal direction as the porosity of the specimen decreases

3.1.2 Coordination orientation

In the consolidation tests, samples become denser and the total area of grain-to-grain contacts increases (Fig. 9). When the porosity is 15%, only about 30% of the contour of a grain is in contact with other grains. When the porosity reaches 3%, more than 80% of the contour of a grain is in contact with other grains. When the porosity of the specimen is high, the axial direction (i.e., 90° in Fig. 9) is the dominating grain-to-grain contact direction. Due to the displacement constraint in the lateral directions, more lateral grain-to-grain contacts occur at later stages of the consolidation tests, and the coordination orientation becomes almost isotropic.

3.1.3 Local solid volume fraction

The evolution of the magnitude of the LSVF vector in the consolidation tests is non-monotonic, as evidenced by Fig. 10b. Usually, a domain polygon contains an entire pore. The larger the pore, the larger the domain polygon, and the higher the number of grains that overlap with this domain polygon. As a result, the magnitude of the LSVF vector is controlled both by the porosity distribution in the domain polygons and by the size of voids. With the decrease in porosity during consolidation, the interval of variation of the LSVF magnitude decreases from 0.25 to 0.13. In other words, the void distribution becomes more uniform. When the porosity of salt rock is 15%, the distribution of probability of the orientation of the LSVF

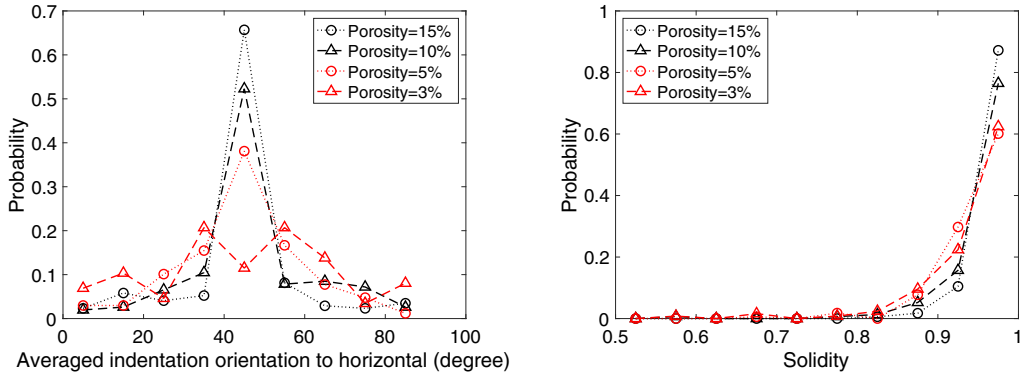

(a) Orientation of the solidity vector **(b)** Magnitude of the solidity vector

Fig. 8 Evolution of the solidity vector during the consolidation tests. The peak of the probability distribution of solidity orientation decreases when the porosity decreases. The mean of solidity also decreases with the decrease in porosity

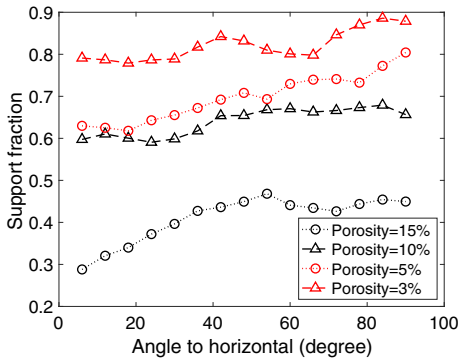

Fig. 9 Evolution of the coordination orientation in the consolidation tests. The support fraction increases and more horizontal contacts occur as the porosity of the specimen decreases

vector (Fig. 10a) is symmetric about 45°; thus, no preferred LSVF orientation is observed. As compression increases, a narrower peak forms, indicating that the LSVF becomes more homogeneous in the sample. The peak shifts to the left, from 45° for a porosity of 15% to 40° for a porosity of 3%. More voids appear in the axial direction around grains, and less voids appear in the lateral direction. In other words, the evolution of the LSVF vector confirms that grains are reorganized in layers of horizontally coordinated grains.

3.2 Cyclic compression tests

3.2.1 Grain morphology

The mean major axis of the grains observed in the microscopic images taken during the cyclic compression tests is slightly less than 400 μm (Fig. 11), which agrees with the size of the salt grains sieved before consolidation (300-355 μm). The aspect ratio usually ranges from 1 to 2, and few elongated grains are observed. The aspect ratio is not significantly affected by the axial strain. There is no significant grain re-orientation during the cyclic compression tests, as shown in Fig. 12.

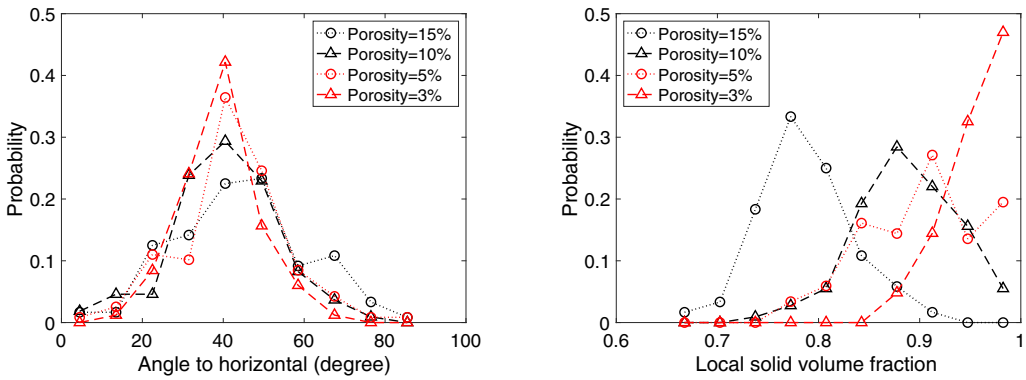

(a) LSVF vector direction **(b)** LSVF vector magnitude

Fig. 10 Evolution of the local solid volume fraction in the consolidation tests. The peak of probability distribution of the LSVF vector direction decreases during the consolidation process. The magnitude of the LSVF vector decreases with the decrease in porosity

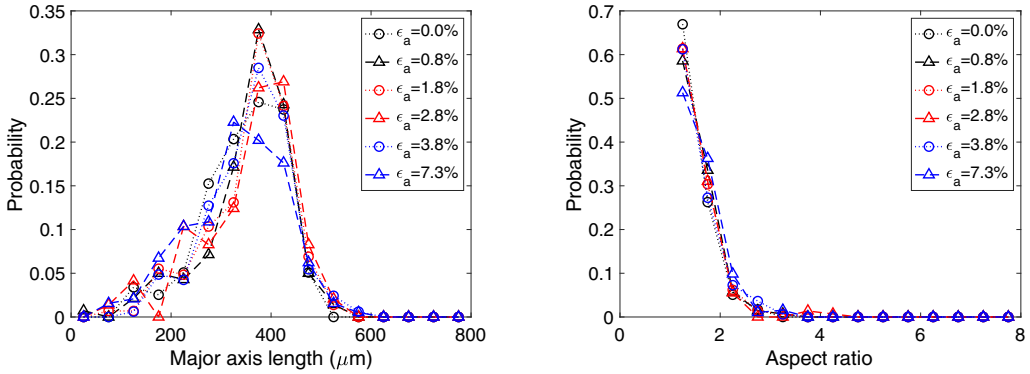

(a) Major axes of grains **(b)** Aspect ratios of grains

Fig. 11 Evolution of the shape of salt grains during the cyclic compression tests. Both the major axes and the aspect ratios of the grains remain stable during the cyclic compression tests

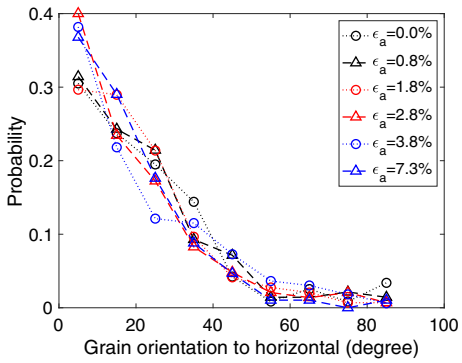

Fig. 12 Evolution of the orientation of the salt grains during the cyclic compression tests. The orientation of the grains is not sensitive to the axial strain of the specimen

We define the indentation ratio as the ratio of the area of one indentation to the area of the convex hull of a grain. According to Fig. 13a, indentation orientations are uniformly distributed within the range 0° to 80°. Few indentation segments are vertical. For larger axial strains, the standard deviation of the indentation orientation probability is larger, i.e., the distribution is more uniform. Based on Fig. 13b, larger indentations appear at larger axial strain. The number of indentations increases with the axial strain, which suggests that more indentations induce more plastic deformation. The mean of the indentation ratio remains almost constant when the axial strain is less than 1.8% and then increases rapidly. We conclude that grain plastic strains start to accumulate when the axial strain reaches 1.8%.

In the cyclic deformation tests, grain deformation by dislocation glide is significantly reduced because the grains have already been hardened during consolidation, and the temperatures and confining pressures of the cyclic deformation tests are very low [11].

The orientation probability distribution loses symmetry slightly when the axial strain increases (Fig. 14). The standard deviation jumps from 16.46 to 19.39 when ϵ_a increases from 1.8% to 2.8%, i.e., the solidity vector starts exhibiting preferential orientations. According to Fig. 14b,

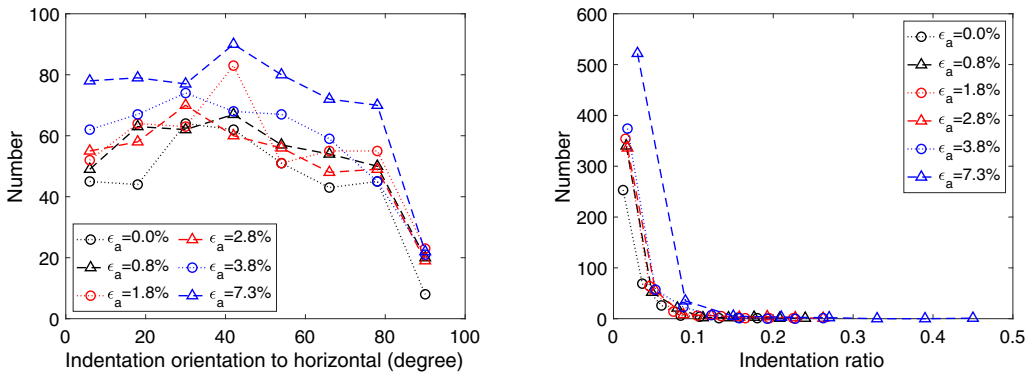

(a) Indentation orientation **(b)** Indentation ratio

Fig. 13 Evolution of the distribution of grain indentations during the cyclic compression tests. The total number of indentations increases with the axial strain of the specimen. The mean indentation ratio starts to increase when the axial strain of specimen is larger than 1.8%

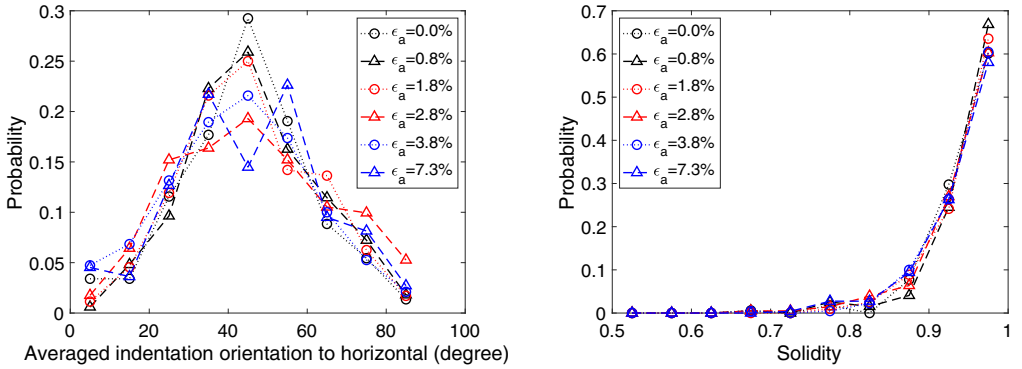

(a) Orientation of the solidity vector **(b)** Magnitude of the solidity vector

Fig. 14 Evolution of the solidity vector during the cyclic compression tests. The peak of the probability distribution of solidity orientation decreases when the axial strain of specimen increases. The mean solidity decreases with the decrease in porosity

the probability distributions of the magnitude of solidity are almost super-imposed for all the different levels of axial strain. When ϵ_a reaches 7.3%, the mean of the magnitude of solidity reduces slightly, which indicates that the area of the indentations increases.

3.2.2 Coordination orientation

The evolution of the probability distribution of the coordination orientation shows that the support fraction decreases when the axial strain increases (Fig. 15). The areas of grain-to-grain contacts reduce because of the redistribution of voids and because of the propagation of intergranular cracks. The slope of the coordination orientation curve is steeper under the larger axial strain. This observation reveals that grains tend to be reorganized into vertical supporting columns, i.e., grain-to-grain contacts are mainly oriented with a normal parallel to the axial (loading) direction. For an axial strain of 7.3%, less than 40% of the grains are in contact with other grains in sub-horizontal directions (with a coordination angle smaller than 20°), while nearly 75% of the grains are coordinated vertically. However, the support fraction of the non-deformed sample ($\epsilon_a = 0\%$) is smaller than the support fractions of samples under $\epsilon_a = 1.8\%$ and $\epsilon_a = 2.8\%$, which contradicts our interpretation. We will explain this apparent contradiction by analyzing normalized fabric descriptors, to account for the difference between 2D and 3D porosities (see Sect. 4.2).

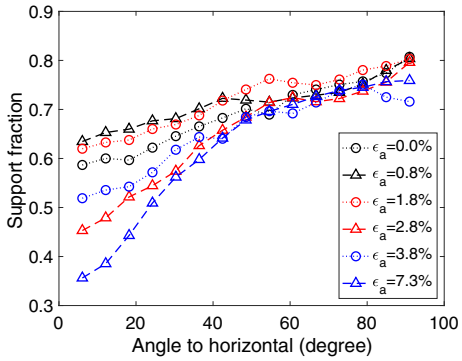

Fig. 15 Evolution of the coordination orientation in the cyclic compression tests. The support fraction of horizontal contacts decreases during the cyclic compression tests, except the specimens with axial strain 0% and 2.8%. The support fraction of vertical contacts is around 0.7 for all specimens with different axial strains

3.2.3 Local solid volume fraction

The evolution of the direction and magnitude of local solid volume fraction (LSVF) vector is shown in Fig. 16a, b, respectively. The magnitude of the peak in Fig. 16a decreases with the increase in the axial strain. When the axial strain is small, the domain polygons of each grain have all similar porosities, i.e., porosity is uniformly distributed, which translates into a peak LSVF orientation angle close to 45°. When the axial strain is larger, the porosity of the domain polygons for each grain is no longer uniform. The probability distribution of the LSVF orientation angle loses its symmetry. This is particularly visible in the sample with ϵ_a = 7.3%, for which polygons characterized by an LSVF angle close to 90° have a higher probability of occurrence (i.e., the line with blue triangle markers is above other lines). This observation confirms the hypothesis of grain re-arrangement in the form of supporting columns of vertically coordinated grains.

The magnitude of LSVF (Fig. 16b) is small when the axial strain is small, i.e., when a few large and isolated pores are observed. When the axial strain increases, large pores collapse, and more small and isolated pores appear. Therefore, the magnitude of the LSVF vector increases when the axial strain increases from 0% to 3.8% (Fig. 16b). Then, because of the propagation of intergranular cracks,

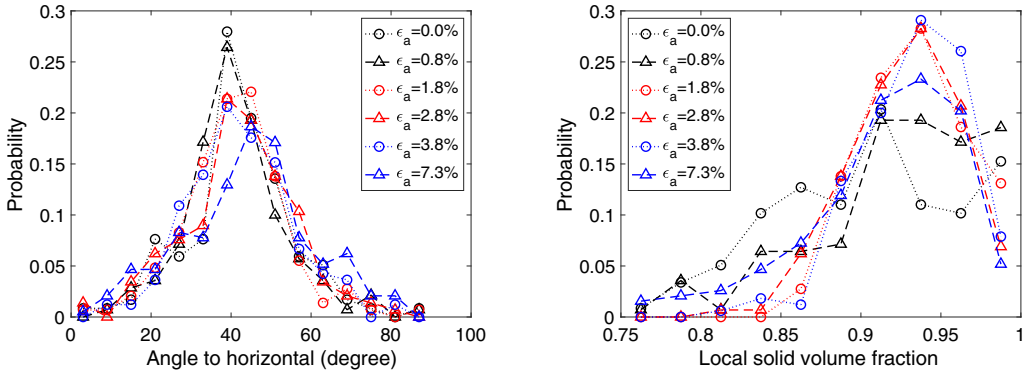

(a) LSVF vector direction **(b)** LSVF vector magnitude

Fig. 16 Evolution of the local solid volume fraction in the cyclic compression tests. The peak of the probability distribution of the LSVF vector direction decreases and moves toward larger angles to the horizontal with the increase in the axial strain. The peak of magnitude of the LSVF vector increases until the axial strain reaches 3.8%. The mean of the magnitude of the LSVF vector decreases for axial strains between 0 and 3.8%, then increases, and then decreases again for axial strains between 3.8 and 7.3%

small pores become connected, thus creating large voids. Thus, the magnitude of the LSVF vector starts to decrease.

3.2.4 Crack length and orientation

The evolution of the distributions of length and orientation of the cracks during the cyclic compression tests is shown in Fig. 17. Following [6], a pore is a void that has a relatively low aspect ratio (quasi-spherical voids) and cracks are characterized by a high aspect ratio (e.g., length to aperture). The cracks initiate at the beginning of the test. Vertical cracks appear first. Cracks in other directions follow, as shown in Fig. 17a. As compression increases, both the length and the number of cracks increase (Fig. 17b). The change in porosity reflects the creation of new porosity through open-mode cracks, and a reduction of porosity through pore closure. The increase in porosity determined from experimental measurements reflects a net increase in porosity because crack opening slightly dominates pore closure. As shown in Fig. 18, the volume of the pores starts by decreasing rapidly. The rate of pore volume reduction stabilizes to a small value when ϵ_a reaches 2%. The volume of opening-mode cracks develops at a slightly increasing rate. When ϵ_a reaches 7%, the opening-mode cracks contribute to more than 20% of the void volume in the sample. Note that the 2D porosity obtained by image analysis is slightly larger than the porosity determined by the mass and volume of salt rock in 3D. This fact does not affect the qualitative interpretations that we made on the evolution of cracks, but we will revisit some of our analyses in Sect. 4.2 to account for the difference between 2D and 3D porosities.

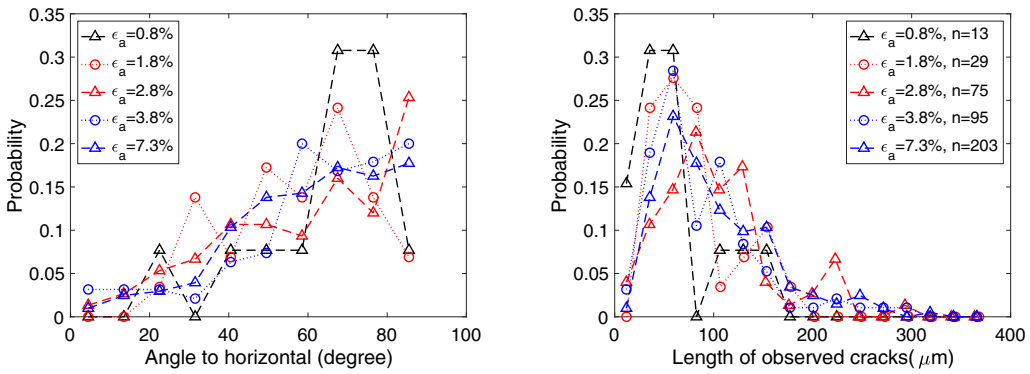

(a) Crack orientations **(b)** Crack lengths

Fig. 17 Orientation and length distributions of the cracks observed in the 2D images obtained at several stages of the cyclic compression tests. The number of cracks (n) is given for each loading stage. Cracks initiate and propagate with the increase in the axial strain. At all stages of the test, there are more cracks oriented vertically than in the other directions

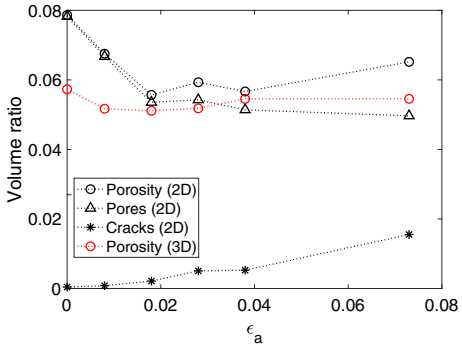

Fig. 18 Distribution of the void volume in the cyclic compression tests. The volume of the cracks increases linearly and the volume of the pores decreases with the accumulation of axial strain

4 Discussion

4.1 Grain deformation

The time-dependent behavior of granular salt is sensitive to the properties of intergranular contacts [37, 48]. Indentations at the surface of salt grains induce a difference of pressure at the intergranular contact planes. The chemical imbalance is restored by dissolution at the contacts under high pressure, diffusion along grain boundaries, and precipitation at the contacts with less pressure [42]. This phenomenon, known as pressure solution, triggers relative sliding displacements between the grains and is very sensitive to the geometry of contacts. Recent studies show that the rate of sliding displacement is inversely proportional to the square of the depth of indentation [27, 40], which indicates that smaller solidity of grains may retard the pressure solution-induced sliding between the contacted grains.

In order to understand the main factors at the origin of salt aggregate deformation during consolidation and compression, we use the 2D solidity vector to calculate the percentage of axial and volumetric deformation that is induced by indentations on the grain surface. The deformation of the salt aggregate is due to both intragranular processes and intergranular processes. Solidity provides a lower bound of grain deformation (intragranular strain), because some grain deformation only results in a loss of convexity or a decrease in circularity, without affecting solidity. For example, consider a cubic packing of equidimensional spheres that, through isotropic consolidation, becomes a cubic packing of cubes; these grains present no concavity, but grain deformation and aggregate deformation are both large. As such, we think that concavity gives a lower bound of deformation. The analysis of the results presented in Fig. 13 shows that the area of the indentations is small compared to that of the grains. Based on this observation, we propose a simple method to estimate the contribution of grain indentation to the deformation of the sample. Let us assume that convex hulls are roughly circular in the 2D images and that indentations are uniformly distributed on the contours of the grains. The relation between the magnitude of the 2D solidity vector, S, and the average depth of the indentations, $\bar{d}$, can then be expressed as:

$$S = 1 - \frac{\sum A_i}{A_s} = 1 - \frac{2\pi R\bar{d}}{\pi R^2} = 1 - \frac{2\bar{d}}{R} \tag{1}$$

where A_i is the area of the ith indentation found on the contour of a grain, and A_s is area of the convex hull of that grain, where here, all grains are assigned an average radius R that is representative of the uniform grain size distribution. The axial strain ϵ_a^g induced by the indentation on the surface of the grain can be expressed as:

$$\epsilon_a^g = \frac{\bar{d}}{R} \tag{2}$$

In the cyclic compression tests, the axial strain induced by grain indentations ϵ_a^g between $\epsilon_a = 0\%$ and $\epsilon_a = 7.3\%$ is found to be equal to 0.5%, which represents only 6.85% of ϵ_a at the final stage of the test (7.3%). The remaining 93.8% is due to grains rearrangements, as discussed in Sect. 3.

Under the same assumption of uniform distribution of indentations, the volumetric strain ϵ_v^g due to the indentation of the grains can be expressed as:

$$\epsilon_v^g = \frac{\delta \sum V_i}{V_s} = \frac{4\pi R^2 \bar{d}}{\frac{4}{3}\pi R^3} = \frac{3\bar{d}}{R} \tag{3}$$

where V_i is the volume of the ith indentation of a grain, and V_s is the volume of the convex hull of that grain. The volumetric deformation due to grain indentations at $\epsilon_a = 7.3\%$ was found to be equal to 1.3% (shrinkage), while the volumetric deformation of the sample was -1.9% (dilation). This observation implies that the volumetric strain of the sample is achieved by the other mechanisms discussed in Sect. 3. For the consolidation tests, the volumetric strain induced by grain indentation at porosity 15%, 10%, 5%, and 3% are, respectively, 2.6%, 5.0%, 7.1%, and 7.9% of the total volumetric strain of the samples. To summarize, despite the simplicity of the grain deformation model adopted here, we can conclude that, in both the consolidation tests and the cyclic compression tests, the axial and volumetric strains of the specimen are mostly due to grain rearrangement, and much less so to grain indentation.

4.2 Normalization of fabric descriptors in the cyclic compression tests

To analyze the evolution of salt microstructure during the cyclic compression tests, specimens are sacrificed at

several stages of the axial strain loading. The initial porosity of the sacrificed samples, noted p_i, ranges between 5.1 and 5.7%, as shown in Table 1. During the compression tests, the sample dilates (i.e., the volumetric strain ϵ_v increases) with the increase in differential stress. According to Sect. 3.2.1, very little changes are noted in grain shape and grain size. Since grain volume changes are negligible, the current porosity of the sample, noted p_c, is calculated from the initial porosity p_i and the current volumetric strain ϵ_v, as follows:

$$p_c = \frac{\epsilon_v + p_i}{\epsilon_v + 1} \tag{4}$$

A discrepancy is noted between p_c and the porosity found by image analysis, noted p_m. In fact, the 3D salt rock sample can be regarded as a stack of 2D microscopic images, in which the thickness of each image is a small constant. 3D porosity can be seen as the mean of the 2D porosities in the stack of images. As we only use the 2D porosity of one microscopic image, a difference between the 2D porosity and the 3D porosity is expected. According to Fig. 17, the porosity obtained by analyzing 2D images is often larger than the porosity of the 3D sample, calculated by estimating the mass density of the sample. As a result, the support fraction calculated from the 2D image analyses is underestimated. We propose a normalization method to correct the error made by using 2D porosities in the cyclic compression tests.

Based on the discussion presented in Sect. 4.1, we consider that the contribution of grain deformation to the deformation of the salt rock specimen is negligible. The coordination orientation is normalized by the current porosity p_c for each compression test. The probability of the normalized coordination orientation is shown in Fig. 19. In samples with ϵ_a equal to 0% and 2.8%, there is a large difference between p_i and p_m; hence, the support fraction increases after normalization. The normalized results confirm the interpretations made in Sect. 3.2.2: During the cyclic compression tests, the overall grain-to-grain contact area reduces and the support fractions line up vertically, forming supporting columns of coordinated grains.

Table 1 Evolution of volumetric parameters in salt rock during the triaxial cyclic loading test

ϵ_a	0%	0.8%	1.8%	2.8%	3.8%	7.3%
p_i	5.7%	5.2%	5.1%	5.2%	5.4%	5.4%
ϵ_v	0.0%	0.0%	0.0%	−0.2%	−0.6%	−1.9%
p_m	7.9%	6.8%	5.6%	5.9%	5.7%	6.5%

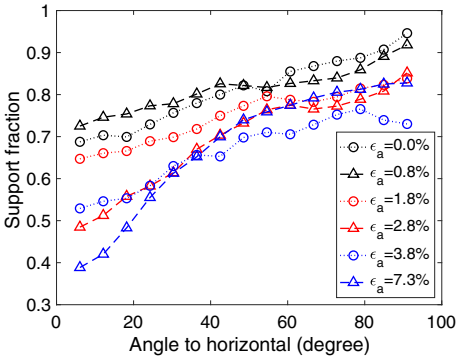

Fig. 19 Evolution of the coordination orientation after normalization in the cyclic compression tests. The support fraction decreases with the accumulation of axial strain. The support fraction of horizontal contacts decreases much faster than the support fraction of vertical contacts, which suggests that grains rearrange to form vertical columns of coordinated grains

The evolution of the magnitude of the LSVF vector after normalization is shown in Fig. 20. The trends are similar to those observed in Fig. 16b. For ϵ_a equal to 1.8%, 2.8%, and 3.8%, curves almost overlap. The distribution of void sizes follows two stages. At the beginning of the test, larger pores collapse, and a significant number of small pores appear. When the axial strain is large, the small pores are connected by intergranular cracks, and large voids appear again.

4.3 Categories of cracks observed in the cyclic compression tests

The cracks observed in the petrographic images acquired during the cyclic compression tests were categorized as intragranular opening-mode cracks and intergranular opening-mode cracks. During the compression tests, both opening-mode cracks and shear-mode cracks are expected

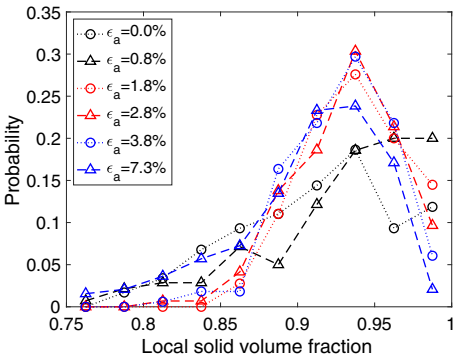

Fig. 20 Evolution of the magnitude of the local solid volume fraction during the cyclic compression tests, after normalization. The peak probability of the magnitude of the LSVF vector increases until the axial strain reaches 2.8%. When the axial strain is larger than 2.8%, the magnitude of the most likely LSVF (at the peak of probability) decreases as the axial strain increases

to initiate and propagate. However, only opening-mode cracks can be observed in the microscopic images. Based on wing crack theory [16], sliding along a crack plane cannot yield displacement without opening a crack (called wing crack) in the tip region of that crack plane. Consequently, opening-mode cracks are expected to occur whenever shear-mode cracks propagate. We infer from this that the observed intergranular opening-mode cracks are wing cracks (this is an idealized "wing-cracks" model). The slip along flaws is accommodated by the opening of cracks or widening of existing open spaces (pores) at grain intersections, and in some cases, pore closure [13].

We developed an algorithm that identifies intergranular shear-mode cracks in the two following cases:

(i) One end of a grain boundary is connected to an intergranular opening-mode crack, and the other end is connected to a void;
(ii) Each end of a grain boundary is connected to a different intergranular opening-mode crack.

We observe very few intragranular cracks, which are all very short. The orientation and length distributions of the intergranular wing cracks (Fig. 21) are in fact very similar to the orientation and length distributions of the observed cracks (Fig. 17). This is because the number of intragranular cracks is limited in the cyclic compression tests. Intergranular shear-mode cracks initiate preferentially at 40° to the horizontal as shown in Fig. 22. With the increase of ϵ_a, the distribution of sliding orientations stabilizes, and intergranular shear-mode cracks propagate along the boundaries of less favorably oriented grains (e.g., grains at $\sim 30°$, with higher normal stress and lower shear stress at the boundaries). A few sub-vertical intergranular shear-mode cracks develop. According to Fig. 21b, the length of the intergranular shear-mode cracks is around 200 μm when ϵ_a is small. A larger axial strain leads to longer intergranular shear-mode cracks and a larger range of length distributions. When ϵ_a is equal to 7.3%, the length of intergranular shear-mode cracks reaches 500 μm.

4.4 Fabric tensors

Fabric tensors are used to describe the evolution of the microstructure in the salt specimens. According to [31], the second-order fabric tensor $\bar{\boldsymbol{F}}$ is expressed as:

$$\bar{F}_{ij} = \int_{\Omega} n_i n_j E(\Omega) \mathrm{d}\Omega \qquad (i,j = x,y,z) \tag{5}$$

where n_x, n_y, n_z are projections of a unit vector $\boldsymbol{n}$ on the Cartesian reference coordinates; Ω is the whole solid angle corresponding to a unit sphere; $E(\Omega)$ is a probability density function (mathematical expectancy). For 2D analyses, the second-order fabric tensor $\boldsymbol{F}$ can be expressed as:

$$F_{ij} = \int_{\theta=0}^{2\pi} n_i n_j E(\theta) \mathrm{d}\theta \qquad (i,j = x,z) \tag{6}$$

$\boldsymbol{F}$ is a symmetric tensor. In order to account for orientation distribution of fabric descriptors, we use the magnitude of the fabric descriptors (noted f_m) as the weight of the orientation of that descriptor (noted θ_m). The components of $\boldsymbol{F}$ are calculated as:

$$F_{xx} = \frac{1}{N} \sum_{m=1}^{N} f_m \sin^2 \theta_m \tag{7}$$

$$F_{xz} = F_{zx} = \frac{1}{N} \sum_{m=1}^{N} f_m \sin \theta_m \cos \theta_m \tag{8}$$

$$F_{zz} = \frac{1}{N} \sum_{m=1}^{N} f_m \cos^2 \theta_m \tag{9}$$

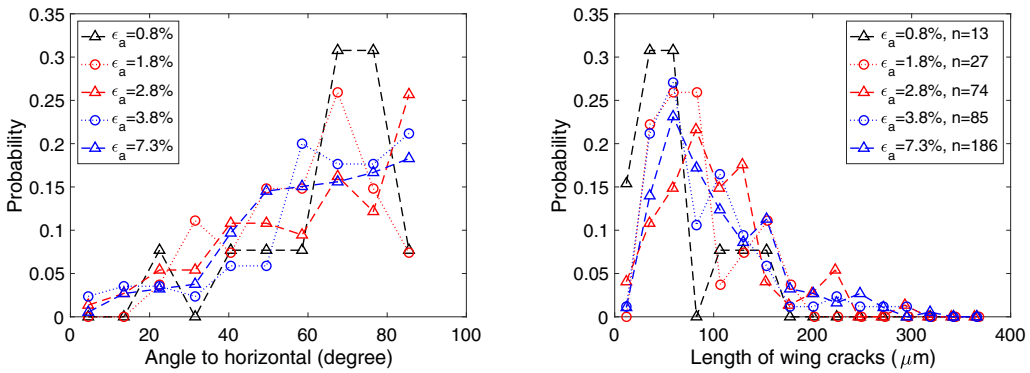

(a) Wing crack orientations **(b)** Wing crack lengths

Fig. 21 Orientation and length distributions of the wing cracks observed in the 2D images obtained at several stages of the cyclic compression tests. Wing cracks initiate and propagate with the increase in the axial strain. There are more wing cracks oriented vertically than in the other directions

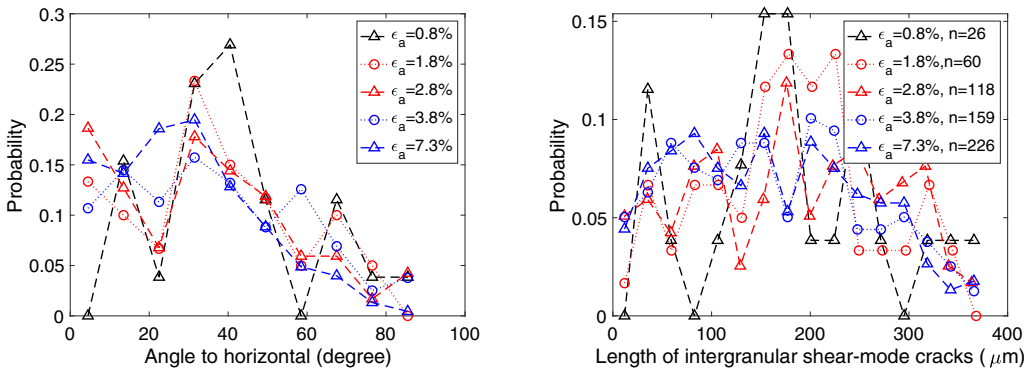

(a) Intergranular shear-mode crack orientations

(b) Intergranular shear-mode crack lengths

Fig. 22 Orientation and length distributions of the intergranular shear-mode cracks at several stages of the cyclic compression tests. There are more intergranular shear-mode cracks oriented horizontally than in the other directions

where f_m is the magnitude of a fabric descriptor for grain m; θ_m is the direction of that fabric descriptor for grain m. Due to the axial symmetry of the samples and loading conditions, F_{xz} and F_{zx} are close to 0. F_{xx} is the component of the fabric tensor in the lateral direction; F_{zz} is the component of the fabric tensor in the axial direction, and F is the trace of the fabric tensor. In 2D: $F = F_{xx} + F_{zz}$.

In the consolidation tests, the compaction of the specimens leads to a larger oedometer modulus and a denser packing of the salt grains (Fig. 23). Solidity decreases due to the inelastic deformation of the grains. Both lateral and axial components of the coordination fabric tensor (C_{xx} and C_{zz}) increase as the porosity of the sample decreases, which indicates that more grain contacts occur at the surface of the grains. This observation is consistent with the observed increase in the odometer modulus. Due to the denser packing of salt rock, a larger LSVF (L) is observed. The discrepancy between L_{xx} and L_{zz} reveals the development of salt rock anisotropy: The sample becomes denser in the lateral direction as porosity decreases.

In the cyclic compression tests, the elastic modulus in the axial direction decreases, while the Poison's ratio increases with the increase in axial strain (Fig. 24). Both components of the solidity fabric tensor (S_{xx} and S_{zz}) are stable, and no obvious anisotropic trend is observed in terms of solidity. The trace of the coordination fabric tensor (C) reaches its lowest point at the highest axial deformation. This means that grains are supported by less neighboring grains, which results in a reduction in the axial elastic modulus. The lateral components of the coordination and LSVF tensors decrease more than the axial components. Physically, that means that grains are less supported in the lateral direction and have more space to move in the specimen. Under a given axial load, it is expected that the displacement of salt grains will be larger than in the initial microstructure (at 0% deformation). Macroscopically, this means that the Poisson's ratio of the specimen has increased.

Based on the orientation distribution of microscopic cracks, we calculated the fabric tensor of wing cracks ($\boldsymbol{D}^w$) and sliding cracks ($\boldsymbol{D}^s$) with Equation 6. $\boldsymbol{D}^w$ and $\boldsymbol{D}^s$ have a unit trace. The evolution of anisotropy induced by microscopic cracks during the cyclic compression tests is shown in Fig. 25. Most wing cracks are vertical. The proportion of lateral wing cracks increases slightly as the axial strain increases (Fig. 25a). At the initial stage of the cyclic compression tests, the distribution of orientation of the sliding cracks is almost isotropic (i.e., D^s_{xx} is close to D^s_{zz}), see Fig. 25b. As the axial strain increases, wing cracks develop predominantly in the lateral direction.

5 Conclusions

In both the consolidation and the cyclic compression tests, the deformation of the specimen is mostly due to grain rearrangement. Practically no crack develops during the consolidation tests, whereas in the cyclic compression tests, intergranular opening-mode cracks propagate due to the development of intergranular shear-mode cracks.

In the consolidation tests, the contribution of grain indentation to the total deformation of the sample increases as the porosity decreases, but it never exceeds 8% of the volumetric deformation of the sample, even at a porosity as low as 3%. When the porosity of the specimen reaches 3%, the aspect ratio and the length of the major axes of the grains increase because of intragranular dislocation glide in the grains. Due to the presence of rigid walls at the lateral boundaries of the sample, lateral grain-to-grain contacts appear and increase in size during the consolidation process. Salt grains reorganize to form horizontal layers of

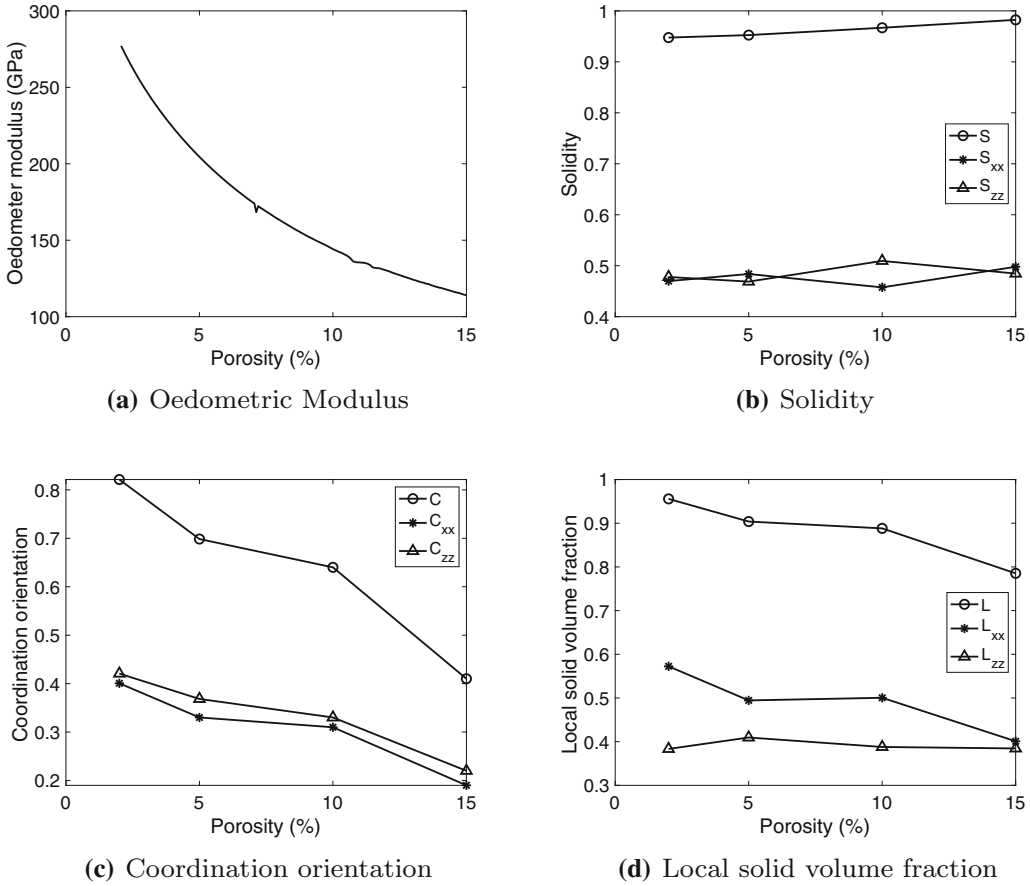

(a) Oedometric Modulus **(b)** Solidity

(c) Coordination orientation **(d)** Local solid volume fraction

Fig. 23 Evolution of the oedometric modulus and of the axial and lateral components of fabric tensors during the consolidation tests. Notation: F_{xx}, F_{zz}: lateral, axial components of fabric tensor $\boldsymbol{F}$. F: trace of $\boldsymbol{F}$: $F = F_{xx} + F_{zz}$. The oedometric modulus is measured directly in the experiments [11]. The oedometric modulus and the components C_{xx}, C_{zz}, and L_{xx} increase with the decrease in porosity. Solidity (S) reduces in the consolidation tests

elongated and coordinated grains. As a result, the orientation distribution of grain indentations is quasi-uniform. The size of the pores reduces and become more uniformly distributed in the specimen. As a result, salt rock microstructure becomes more homogeneous.

In the cyclic compression tests, the changes in grain shape and size are negligible, and dislocation glide is significantly reduced. The deformation of the grains is mainly induced by indentations on the surface of the grains. The number and the area of the indentations increase with the increase in the axial strain, which causes an accumulation of plastic deformation. Large plastic deformation occurs in the axial loading direction. Most of the specimen deformation is due to grain rearrangement. Due to the redistribution of grains and the propagation of intergranular cracks, grain-to-grain contact areas reduce. The grain-to-grain contacts occur mainly in the axial direction, and a larger local solid volume fraction is observed in the axial direction of the grains. These observations indicate that grains tend to be reorganized into vertical columns of coordinated grains. When the axial strain is small, a few large and isolated pores are observed. Due to the increase in differential compressive stress, the larger pores collapse and more small and isolated pores appear in the sample. Then, because of the propagation of the intergranular cracks, small pores become connected and form large voids, which explains the non-monotonic evolution of the void pore distribution. Very few, short intragranular cracks are noted. Intergranular opening-mode cracks are observed. We propose an idealized wing crack model which allows identifying grain boundaries where intergranular shear-mode cracks develop. Intergranular opening-mode cracks tend to develop in the axial direction, while intergranular shear-mode cracks propagate preferentially in sub-horizontal directions. The volume of intergranular opening-mode cracks increases linearly with the axial strain.

We analyzed the orientation distributions of the fabric tensors of solidity, coordination, and local solid volume fraction. In the consolidation tests, the local solid volume fraction increases more in the lateral direction than in the axial direction, which indicates that salt rock becomes much denser laterally under compaction. The oedometer

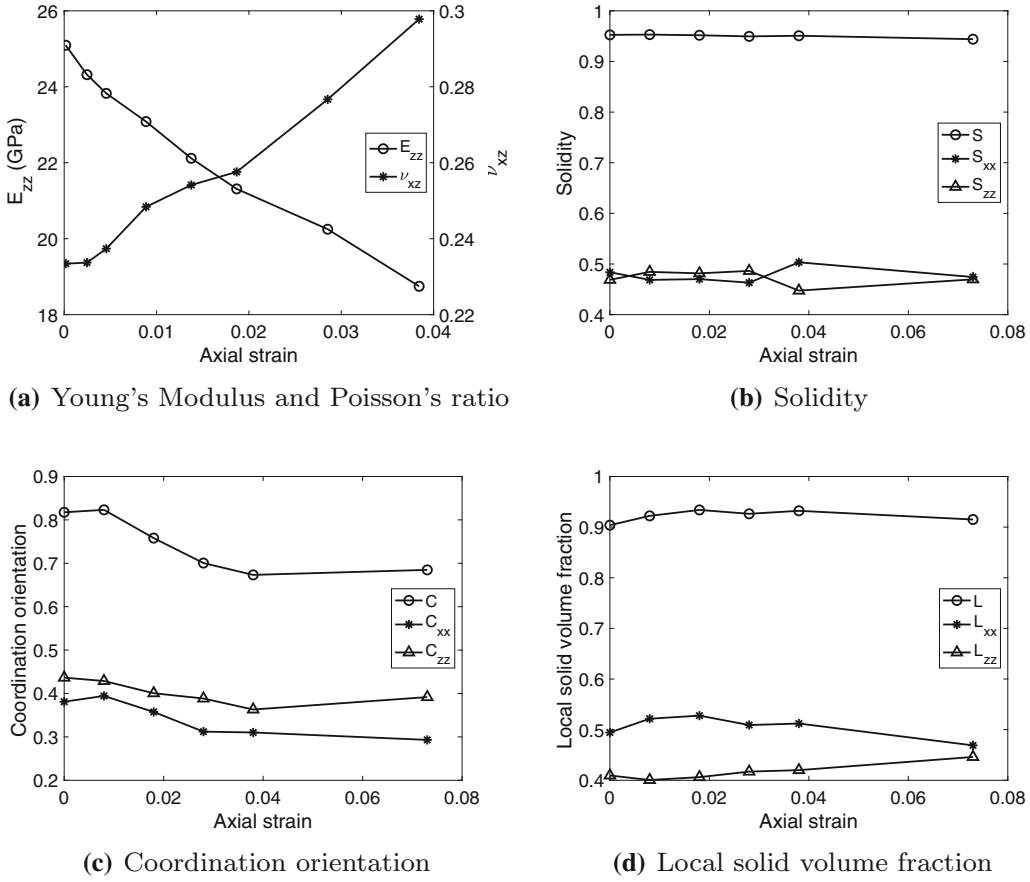

(a) Young's Modulus and Poisson's ratio **(b)** Solidity

(c) Coordination orientation **(d)** Local solid volume fraction

Fig. 24 Evolution of elastic properties and of axial and lateral components of fabric tensors during the cyclic compression tests. Notation: F_{xx}, F_{zz}: lateral, axial components of fabric tensor $\boldsymbol{F}$. F: trace of $\boldsymbol{F}$: $F = F_{xx} + F_{zz}$. The Young's Modulus and the Poisson's ratio are measured directly in the experiments [11]. The Young's modulus (E_{zz}) and the magnitude of the coordination orientation tensor (C) decrease with the accumulation of axial strain. The Poisson's ratio (v_{xz}) increases and the solidity (S) remains stable. A slight decrease of L_{xx} and a slight increase of L_{zz} occur during the cyclic compression tests

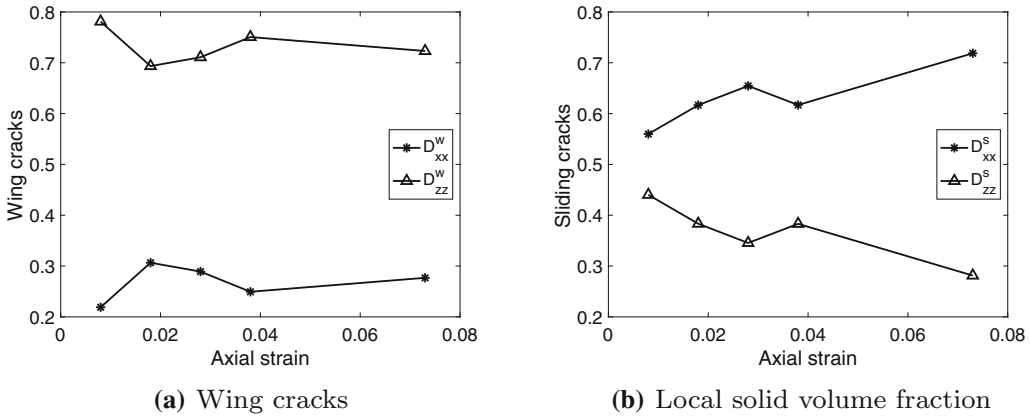

(a) Wing cracks **(b)** Local solid volume fraction

Fig. 25 Evolution of axial and lateral components of crack fabric tensors during the cyclic compression tests. D^w_{xx} and D^w_{zz} are the lateral and axial components of the wing crack fabric tensor $\boldsymbol{D}^w$. D^s_{xx} and D^s_{zz} are the lateral and axial components of sliding crack fabric tensor $\boldsymbol{D}^s$

modulus increases. In the cyclic compression tests, the lateral components of coordination and local solid volume fraction decrease, which results in an increase in the Poisson's ratio.

The fabric descriptors used in this work allow a better quantification and understanding of halite deformation processes. The analysis of microstructure sheds light on the design and safety analysis of the geological storage

facilities in salt rock. The proposed fabric descriptors can also be used in other types of rocks encountering similar deformation mechanisms.

Acknowledgements This work was funded by the US National Science Foundation, under grants CMMI 1362004/1361996 (Collaborative research: Linking Salt Rock Deformation Regimes to Microstructure Organization) and CMMI 1552368 (CAREER: Multiphysics Damage and Healing of Rocks for Performance Enhancement of Geo-Storage Systems—A Bottom-Up Research and Education Approach).

Compliance with ethical standards

Conflict of interest The authors declare that they have no conflict of interest.

References

1. Al-Raoush R, Alsaleh M (2007) Simulation of random packing of polydisperse particles. Powder Technol 176(1):47–55
2. Al-Raoush R, Alshibli KA (2006) Distribution of local void ratio in porous media systems from 3d x-ray microtomography images. Phys A Stat Mech Appl 361(2):441–456
3. Arson C (2020) Micro–macro mechanics of damage and healing in rocks. Open Geomech 2:1–41
4. Arson C, Xu H, Chester FM (2012) On the definition of damage in time-dependent healing models for salt rock. Géotech Lett 2(2):67–71
5. Bauer SJ, Song B, Sanborn B (2019) Dynamic compressive strength of rock salts. Int J Rock Mech Min Sci 113:112–120
6. Brace W, Paulding B Jr, Scholz C (1966) Dilatancy in the fracture of crystalline rocks. J Geophys Res 71(16):3939–3953
7. Cavarretta I (2009) The influence of particle characteristics on the engineering behaviour of granular materials. PhD thesis, Imperial College London (University of London)
8. Chester F (1988) Temperature and rate dependence of friction for faults. Eos Trans AGU 69:471
9. Clayton C, Abbireddy C, Schiebel R (2009) A method of estimating the form of coarse particulates. Geotechnique 59(6):493–501
10. Dai S, Shin H, Santamarina JC (2016) Formation and development of salt crusts on soil surfaces. Acta Geotech 11(5):1103–1109
11. Ding J (2019) Grain boundary processes, anelasticity, and test of the effective stress law for semibrittle deformation of synthetic salt-rocks. PhD thesis, Texas A & M University
12. Ding J, Chester FM, Chester JS, Zhu C, Arson C (2017) Microcrack network development in salt-rock during cyclic loading at low confining pressure. In: Proceedings of the 51st US rock mechanics/geomechanics symposium
13. Ding J, Chester FM, Chester JS, Zhu C, Arson C, et al. (2016) Mechanical behavior and microstructure development in consolidation of nominally dry granular salt. In: Proceedings of the 50th US rock mechanics/geomechanics symposium. American Rock Mechanics Association
14. Fonseca J, O'Sullivan C, Coop MR, Lee P (2013) Quantifying the evolution of soil fabric during shearing using directional parameters. Géotechnique 63(6):487–499
15. Frost J, Kuo C (1996) Automated determination of the distribution of local void ratio from digital images. Geotech Test J 19(2):107–117
16. Griffith A (1924) The theory of rupture. First Int Cong Appl Mech, pp 55–63
17. Guida G, Viggiani GM, Casini F (2020) Multi-scale morphological descriptors from the fractal analysis of particle contour. Acta Geotech 15(5):1067–1080
18. Hasan A, Alshibli K (2010) Experimental assessment of 3d particle-to-particle interaction within sheared sand using synchrotron microtomography. Géotechnique 60(5):369
19. Kanatani K (1984) Distribution of directional data and fabric tensors. Int J Eng Sci 22(2):149–164
20. Katsman R, Aharonov E, Haimson B (2009) Compaction bands induced by borehole drilling. Acta Geotech 4(3):151–162
21. Kröhn KP, Zhang CL, Czaikowski O, Stührenberg D, Heemann U (2015) The compaction behaviour of salt backfill as a thm-process. In: Proceedings of 8th conference on mechanical behavior salt (SaltMech8), pp 49–59
22. Krumbein WC, Sloss LL (1963) Stratigraphy and sedimentation. Technical report
23. Kuo C (1995) Quantifying the fabric of granular materials: an image analysis approach
24. Lai Z, Chen Q (2019) Reconstructing granular particles from x-ray computed tomography using the tws machine learning tool and the level set method. Acta Geotech 14(1):1–18
25. Linckens J, Zulauf G, Hammer J (2016) Experimental deformation of coarse-grained rock salt to high strain. J Geophys Res Solid Earth 121(8):6150–6171
26. Liu J, Xie H, Hou Z, Yang C, Chen L (2014) Damage evolution of rock salt under cyclic loading in unixial tests. Acta Geotech 9(1):153–160
27. Liu Z, Zhou C, Li B, Zhang L, Liang Y (2019) Effects of grain dissolution-diffusion sliding and hydro-mechanical interaction on the creep deformation of soft rocks. Acta Geotech 15:1–11
28. Madadi M, Tsoungui O, Lätzel M, Luding S (2004) On the fabric tensor of polydisperse granular materials in 2d. Int J Solids Struct 41(9–10):2563–2580
29. Oda M (1977) Co-ordination number and its relation to shear strength of granular material. Soils Found 17(2):29–42
30. Oda M (1982) Fabric tensor for discontinuous geological materials. Soils Found 22(4):96–108
31. Oda M, Nakayama H (1989) Yield function for soil with anisotropic fabric. J Eng Mech 115(1):89–104
32. Palmer S, Barton M (1987) Porosity reduction, microfabric and resultant lithification in UK uncemented sands. Geol Soc Lond 36(1):29–40
33. Paniagua P, Fonseca J, Gylland A, Nordal S (2018) Investigation of the change in soil fabric during cone penetration in silt using 2d measurements. Acta Geotech 13(1):135–148
34. Pouragha M, Eghbalian M, Wan R (2020) Micromechanical correlation between elasticity and strength characteristics of anisotropic rocks. Int J Rock Mech Min Sci 125:104154
35. Raj R, Ashby M (1971) On grain boundary sliding and diffusional creep. Metall Trans 2(4):1113–1127
36. Rutter E (1983) Pressure solution in nature, theory and experiment. J Geol Soc 140(5):725–740
37. Shen X, Arson C (2019a) An isotropic self-consistent homogenization scheme for chemo-mechanical healing driven by pressure solution in halite. Int J Solids Struct 161:96–110
38. Shen X, Arson C (2019b) Simulation of salt cavity healing based on a micro-macro model of pressure-solution. Pet Geosci 25:251–257
39. Shen X, Arson C, Ding J, Chester FM, Chester JS (2020a) Mechanisms of anisotropy in salt rock upon microcrack propagation. Rock Mech Rock Eng. https://doi.org/10.1007/s00603-020-02096-1

40. Shen X, Ding J, Arson C, Chester JS, Chester FM (2020b) Micromechanical modeling for rate-dependent behavior of salt rock under cyclic loading. Int J Numer Anal Methods Geomech
41. Shi J, Guo P (2018) Fabric evolution of granular materials along imposed stress paths. Acta Geotech 13(6):1341–1354
42. Spiers C, Schutjens P, Brzesowsky R, Peach C, Liezenberg J, Zwart H (1990) Experimental determination of constitutive parameters governing creep of rocksalt by pressure solution. Geol Soc Lond 54(1):215–227
43. Su D, Yan W (2019) Prediction of 3D size and shape descriptors of irregular granular particles from projected 2D images. Acta Geotech 15:1–23
44. Taylor MA (2002) Quantitative measures for shape and size of particles. Powder Technol 124(1–2):94–100
45. Thornton C (2000) Numerical simulations of deviatoric shear deformation of granular media. Géotechnique 50(1):43–53
46. Tong Z, Fu P, Zhou S, Dafalias YF (2014) Experimental investigation of shear strength of sands with inherent fabric anisotropy. Acta Geotech 9(2):257–275
47. Urai JL, Spiers CJ, Zwart HJ, Lister GS (1986) Weakening of rock salt by water during long-term creep. Nature 324(6097):554–557
48. Urai J, Spiers C (2007) The effect of grain boundary water on deformation mechanisms and rheology of rocksalt during long-term deformation. In: Proceedings of the 6th conference and mechnical behaviour of salt, pp 149–158
49. Vangla P, Roy N, Gali ML (2018) Image based shape characterization of granular materials and its effect on kinematics of particle motion. Granul Matter 20(1):6
50. Ventouras K, Coop M (2009) On the behaviour of thanet sand: an example of an uncemented natural sand. Géotechnique 59(9):727–738
51. Wadell H (1933) Sphericity and roundness of rock particles. J Geol 41(3):310–331
52. Wang Y, Mok C (2008) Mechanisms of small-strain shear-modulus anisotropy in soils. J Geotech Geoenviron Eng 134(10):1516–1530
53. Wiebicke M, Andò E, Viggiani G, Herle I (2020) Measuring the evolution of contact fabric in shear bands with x-ray tomography. Acta Geotech 15(1):79–93
54. Zhang G, Li Y, Yang C, Daemen JJ (2014) Stability and tightness evaluation of bedded rock salt formations for underground gas/oil storage. Acta Geotech 9(1):161–179
55. Zheng J, He H, Alimohammadi H (2020) Three-dimensional wadell roundness for particle angularity characterization of granular soils. Acta Geotech pp 1–17
56. Zhu C, Arson C (2015) A model of damage and healing coupling halite thermo-mechanical behavior to microstructure evolution. Geotech Geol Eng 33(2):389–410